Journal of The Electrochemical Society, **158** (3) B290-B296 (2011)
0013-4651/2011/158(3)/B290/7/$28.00 © The Electrochemical Society

Evaluation of Several Carbon-Supported Nanostructured Ni-Doped Manganese Oxide Materials for the Electrochemical Reduction of Oxygen

Amanda C. Garcia,[a,b] Alberto Diaz Herrera,[b] Edson A. Ticianelli,[a,*] Marian Chatenet,[b,*,z] and Christiane Poinsignon[b]

[a]*Instituto de Química de São Carlos, Universidade de São Paulo, CP 780 13560-970 São Carlos, São Paulo, Brazil*
[b]*Laboratoire d'Electrochimie et de Physico-chimie des Matériaux et des Interfaces LEPMI-Phelma, UMR 5631CNRS/Université de Grenoble, BP 75, 38402 Saint Martin d'Hères Cedex, France*

Physical and electrochemical properties of nanostructured Ni-doped manganese oxides (MnO_x) catalysts supported on different carbon powder substrates were investigated so as to characterize any carbon substrate effect toward the oxygen reduction reaction (ORR) kinetics in alkaline medium. These $NiMnO_x$/C materials were characterized using physicochemical analyses. Small insertion of Ni atoms in the MnO_x lattice was observed, which consists of a true doping of the manganese oxide phase. The corresponding $NiMnO_x$ phase is present in the form of needles or agglomerates, with crystallite sizes in the order of 1.5–6.7 nm (from x-ray diffraction analyses). Layered manganite (MnOOH) phase has been detected for the Monarch1000-supported $NiMnO_x$ material, while different species of MnO_x phases are present at the E350G and MM225 carbons. Electrochemical studies in thin porous coating active layers in the rotating ring-disk electrode setup revealed that the MnO_x catalysts present better ORR kinetics and electrochemical stability upon Ni doping. The ORR follows the so-called peroxide mechanism on MnO_x/C catalysts, with the occurrence of minority HO_2^- disproportionation reaction. The HO_2^- disproportionation reaction progressively increases with the Ni content in $NiMnO_x$ materials. The catalysts supported on the MM225 and E350G carbons promote faster disproportionation reaction, thus leading to an overall four-electron ORR pathway.
 [DOI: 10.1149/1.3528439]

Manuscript submitted September 16, 2010; revised manuscript received November 29, 2010. Published January 3, 2011.

One of the most studied processes in electrochemistry is the cathodic reduction of molecular oxygen, either in alkaline or in acid solutions, due to its importance in fuel cells[1] and metal-air batteries.[2] Platinum is known to be the best electrocatalyst for the oxygen reduction reaction (ORR) in an alkaline fuel cell cathode,[3] but for simple reasons such as cost and because Pt suffers gradual decrease in activity combined with limited stability in strong alkaline media,[4] non-noble metal electrocatalysts have retained the focus of the scientific community for a long time.[5,6] The main challenge related to the development of highly active catalysts for the ORR is to obtain a material capable of achieving the complete reduction process, where a four-electron transfer per O_2 is involved. However, some of the catalysts reported in the literature accelerate a two-electron reduction of O_2 to produce H_2O_2,[7] which is a severe disadvantage.

Manganese oxides are among the most widely used catalysts employed at the cathode of alkaline metal-air batteries,[8-12] thanks to their sufficient (electro)chemical stability, low cost, and rather high activity toward the ORR.[13,14] One of the functions of these oxides is to perform the decomposition of hydrogen peroxide, which may be formed during the electrochemical reduction of oxygen.[12] The process consists of a disproportionation mechanism, overall driving the ORR to follow the complete four-electron reduction pathway. As primary battery materials,[15] manganese oxides also have the ability to absorb or deliver a high quantity of charge in a short time; such a process, known as the flywheel effect, can advantageously be used in the air-cathode of fuel cells, as demonstrated by Vondrák et al.[16]

Previous studies have shown that nanostructured Ni(II)-doped MnO_x nanoparticles supported on high area carbon exhibit remarkable catalytic activity for the oxygen reduction.[16,17] The four-electron ORR pathway is favored on such materials, probably because the doping transition metal stabilizes an intermediate Mn^{III}/Mn^{IV} phase, which enhances the oxygen bond splitting.[18] Such a feature renders them very attractive electrocatalysts for the air-cathode of an alkaline fuel cell (AFC).

In this work, the catalytic activity of Ni-doped MnO_x catalysts supported on various carbon powder substrates was investigated so as to characterize the effects of these substrates toward the $NiMnO_x$ catalytic properties for the ORR in alkaline medium. Studies were conducted for several Ni-doping levels into the carbon-supported MnO_x lattice. The materials were thoroughly characterized using several techniques, including x-ray diffraction (XRD), high resolution transmission electron microscopy (HRTEM) coupled with chemical analyses [x-ray energy-dispersive spectroscopy (X-EDS)] and elemental analyses [inductively coupled plasma-atomic emission spectroscopy (ICP-AES)]. Electrochemical studies comprised the use of thin porous coating layers (TPC) formed with the carbon-supported electrocatalysts and the rotating disk electrode (RDE) technique in O_2-containing and argon-purged alkaline electrolytes.

Experimental

Preparation of the Ni-doped MnO_x/C catalysts.— The synthesis of the carbon-supported MnO_x materials is derived from that described by Bezdicka et al.[19] Briefly, the procedure consists of a mild hydrothermal reaction between Mn^{VII} and Mn^{II} in the presence of high surface area carbon, at controlled *p*H and temperature. More specifically, the $NiMnO_x$/C materials were obtained by suspending the desired amount of the carbon black powder in an aqueous solution of $KMnO_4$ and $MnSO_4$ (Merck), to reach the targeted Mn loading. The suspension was maintained at a controlled temperature (80°C) for 15 min, and then the MnO_x/C was filtered and dried at 110°C. To prepare the Ni-doped catalysts, a solution of $Ni(NO_3)_2{\cdot}6H_2O$ (Merck) was added prior to the permanganate addition. All the MnO_x-based catalysts were prepared with a nominal Mn/(C + Mn + O + Ni) load of around 20 wt % at the time of their syntheses. The carbon powders used for the catalyst preparation were the Monarch 1000 (M1000, Cabot) and MM225 (acetylene black) or E350G (ENSACO conductive carbon black), both from Timcal. The specific surface areas of these materials are presented in Table I.

Physicochemical characterizations of the carbon-supported MnO_x/C-based materials.— The Ni-doped MnO_x/C electrocatalysts were characterized using XRD experiments on a Philips TW 1730 vertical goniometer/diffractometer equipped with a diffracted-beam

* Electrochemical Society Active Member.
z E-mail: Marian.Chatenet@grenoble-inp.fr

Table I. Values of the specific surface of the different substrates.

Carbon	Specific surface ($m^2\ g^{-1}$)
M1000	343
MM 225	660
E350G	770

monochromator, using Fe Kα radiation and recalculated for the Cu Kα radiation. From these spectra, the MnO_x phases and average crystallite sizes were obtained.

The "local" particles' morphology, shape, and Ni:Mn composition distributions were investigated using HRTEM (JEOL 2010, Consortium des Moyens techniques Communs, Grenoble-INP, CMTC) equipped for chemical analyses (X-EDS). For the local chemical analyses, the X-EDS spectra were obtained by lowering the electron beam down to nanometric size, so as to monitor only the fluorescence of the desired area of the sample.

The overall loadings of each component on the $NiMnO_x$/C electrocatalysts were obtained from ICP-AES analyses after digestion of the $NiMnO_x$/C powders in concentrated *aqua regia*, as described in Ref. 20. Coupling these loading data with those from XRD and transmission electron microscopy (TEM) enabled to evaluate the approximate active area of the electrocatalysts and thus to determine the specific activity (SA, current divided by the specific area of the electrocatalyst) for our various samples. The mass activities (MA) were also calculated in two different ways: The first assumes the active component of the $NiMnO_x$/C electrocatalysts is MnO_2, while the second uses the mass of MnO_2 + Ni as active component.

Electrochemical characterization of the carbon-supported MnO_x/C-based materials.— A glassy carbon disk was used as a substrate to prepare active layers of the desired catalysts.[21] The disk consisted of a glassy carbon rod (ϕ = 5 mm, geometric area = 0.196 cm^2).[22] For the preparation of the catalytic layer, initially, 12.5 mg of the MnO_x/C or $NiMnO_x$/C powders was suspended in a mixture containing 1 mL of water, 0.6 mL of ethanol, and 20 μL of a Nafion solution (5 wt % in low aliphatic alcohol, from DuPont). After ultrasonic homogenization, 20 μL of this ink was deposited on the top of the glassy carbon electrode, and the solvent was then evaporated at room temperature.

In this work, the rotating disk electrode (EDT 101, Radiometer Copenhagen) measurements were performed in 1.0 M NaOH solutions (Suprapur, Merck), prepared with (18.2 MΩ cm, 3 ppb) water (Millipore, Elix + Milli-Q gradient). The electrochemical cell was used in a four-electrode configuration, containing the disk working electrode, a gold foil counter electrode, a gold sphere auxiliary electrode, and a Hg–HgO in 1.0 M NaOH reference electrode (+0.1 V vs normal hydrogen electrode (NHE), Radiometer Analytical). The electrochemical experiments were conducted with a computer-controlled multichannel potentiostat (VMP2, Bio-Logic Science Instruments). The cyclic voltammetry (CV) was carried out after degassing the solution with argon, in the range from 0.2 to − 0.5 V vs NHE. The oxygen reduction experiments were performed at v = 5 mV s^{-1} after saturation of the electrolyte with oxygen; the oxygen concentration was kept constant at its saturation value by permanent O_2-bubbling. Prior to each voltammetric cycle, the potential was kept for 2 min at the starting potential, 0.2 V vs NHE, to ensure an identical initial state of surface for the $NiMnO_x$/C materials in all experiments. In that extent, it is wise to note that the $NiMnO_x$/C materials were not prereduced prior to the ORR characterizations.

The overall number of electrons exchanged per oxygen molecule was estimated from the limiting diffusion current density plateaus, using the classical Levich equation[23]

$$i_d = B\omega^{1/2} \quad [1]$$

where i_d is the limiting diffusion current, B is the Levich coefficient

$$B = 0.62nFAD^{2/3}\nu^{-1/6}C^* \quad [2]$$

where n is the number of electrons involved in the reaction, D = 1.56 × 10^{-5} $cm^2\ s^{-1}$ is the oxygen diffusion coefficient,[24,25] C^* = 8.8 × 10^{-7} mol cm^{-3} is the oxygen solubility in the solution,[24,25] ν = 1.19 × 10^{-2} $cm^2\ s^{-1}$ is the NaOH solution cinematic viscosity,[26] all at 25°C, and ω (rad s^{-1}) is the RDE revolution speed.

Results and Discussion

Chemical and physical characterizations of the carbon-supported MnO_x-based materials.— The composition of the doped manganese oxide nanoparticles was evaluated by ICP-AES (on a global basis). These results are shown in Table II. In all cases, the actual loads of Mn in the catalysts vary in the range of 8.6–17.9 wt % of Mn, while the Ni-doping loads range from 0.18 to 2.2 wt %. The XRD results presented below will enable determination of whether the presence of Ni results from some insertion of the Ni atoms in the MnO_x structure or from the generation of a Ni-based phase. There were some changes of the $NiMnO_x$ load on the support depending on the carbon nature, with the average numbers being 18 ± 2, 24 ± 7, and 22 ± 2 wt % $NiMnO_x$ for C = M1000, MM225, and E350G, respectively (Table II). Assuming the composition of the catalytic suspension used to prepare the thin porous coatings on the glassy carbon RDE tip (see the next section), these figures correspond to $NiMnO_x$ loads per geometric area of the RDE tip varying as follows: 144 ± 16, 193 ± 54, and 173 ± 14 μg cm^{-2} for $NiMnO_x$/M1000, $NiMnO_x$/MM225, and $NiMnO_x$/E350G, respectively.

Table II. Composition (obtained by ICP-AES analyses) and crystallite sizes (d_{XRD}, measured from powder XRD) for the various $NiMnO_x$-based materials. The wt % MnO_2 were calculated assuming that each Mn atom is combined with two O atoms to form a MnO_2 moiety.

Catalyst/carbons	Composition				d_{XRD} (nm)
	wt % Ni	wt % Mn	wt % MnO_2	wt % MnO_2 + Ni	
M1000-2.0 g Ni	2.2	8.6	13.7	15.9	2.1
M1000-1.0 g Ni	1.3	9.6	15.2	16.5	1.8
M1000-0.5 g Ni	0.9	10.4	16.5	17.4	2.0
M1000-0.3 g Ni	0.7	11.4	18.0	18.7	1.5
M1000-0.2 g Ni	0.5	11.6	18.4	18.9	1.8
M1000-0.1 g Ni	0.3	13.2	21.0	21.3	2.3
M1000-0.0 g Ni	—	—	—	—	7.2
MM225-0.2 g Ni	0.7	17.9	28.3	29.0	5.7
MM225-0.1 g Ni	0.2	12.1	19.2	19.4	6.2
E350G-0.2 g Ni	0.3	12.8	20.2	20.5	6.4
E350G-0.1 g Ni	0.2	14.4	22.7	22.9	6.7

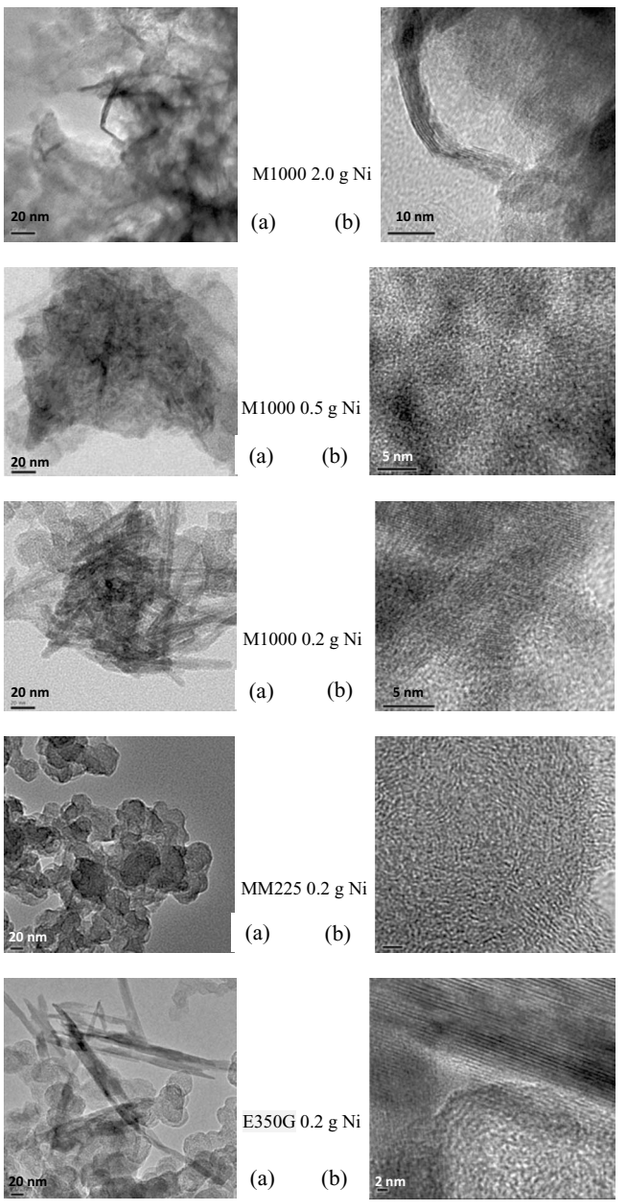

Figure 1. (a) TEM and (b) HR-TEM images of $NiMnO_x$/C electrocatalyst dispersed in the M1000, MM225, and E350G powder.

Figure 1 show representative TEM and HRTEM images for the $NiMnO_x$/C electrocatalysts dispersed onto the M1000, MM225, and E350G powders. It is noted that the particles of the $NiMnO_x$ materials do not exhibit very good dispersion over the carbon powder (Fig. 1a). The structure of the oxide phases changes depending on the carbon type and Ni load; they are in the form of highly oriented nanocrystalline needles for the M1000 materials for Ni loads lower than 0.5 g, while for MM225 (both Ni loads) and for M1000 with Ni loads above 0.5 g, nanocrystalline agglomerates with only short-range ordering seem to be formed. In the case of E350G the existence of a mixed situation is evidenced at all Ni loads.

Figure 1b presents higher resolution images, showing that the structures of the Mn oxide phases are highly monocrystalline, but present several surface orientations. Due to the non-negligible extent of particles size/shape heterogeneity, the results of TEM or HRTEM do not enable the determination of any average particle size. However, from these TEM analyses it is estimated that the nanocrystalline needles, when present, exhibit diameters on the order of 5 nm and lengths close to 100 nm.

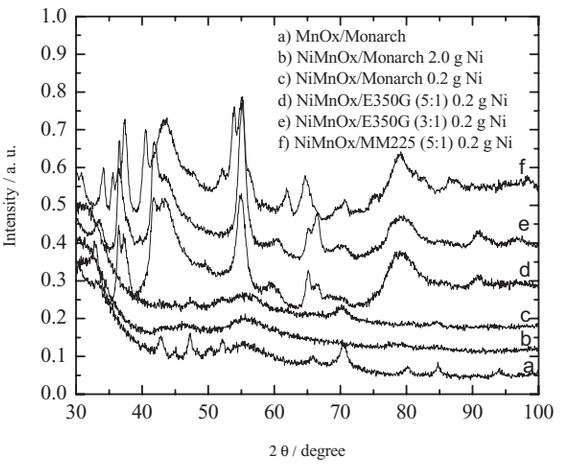

Figure 2. Example of XRD for representative materials: M1000, E350G, and MM225 catalysts with various Ni contents.

Some XRD patterns obtained for the $NiMnO_x$/C materials are shown in Fig. 2. Various crystallographic structures are observed as a function of the Ni content, with some drastic changes observed when the MM225 and E350G carbons are used instead of the Monarch 1000. The XRD spectra show interlayer reflections typical of layered manganite (MnOOH: peaks at $2\theta = 45$ and 55°) in the case of M1000-supported $NiMnO_x$, while for the E350G and MM225 carbons, the XRD spectra show different species of MnO_x as main phases, with the absence of MnOOH. No isolated nickel phase was detected for the M1000-supported $NiMnO_x$ samples (it was not detected on a local basis by TEM + X-EDS either), indicating that the Ni^{2+} divalent cations were indeed inserted into the MnO_x crystalline structure (which consists of a true doping). In the cases of the E350G and MM225 carbons, the presence of negligible quantities of NiO_2 and NiC phases is evidenced by XRD, as indicated by the diffraction peaks at 38, 40, 46, and 52°. Disregarding this latter (very minor) bias, the Ni-adjunction overall consists of a true insertion within the MnO_x/C lattice, as forecast.[19]

The average crystallite sizes were estimated using the Scherrer equation,[27] the results being presented in Table II. For the M1000 materials, the calculation was attempted for the diffraction peak at $2\theta = 55°$, which corresponds to the MnOOH phase. For the MM225 and E350G materials, the peaks at $2\theta = 65$ and 55° were considered, because these two reflexions correspond to the MnO_2 phase in larger amount in these cases. The crystallite sizes were in the range of 1.5–6.7 nm for all $NiMnO_x$/C catalysts.

Electrochemical characterizations of the MnO_x/C-based catalysts.— Figure 3 displays representative cyclic voltammograms acquired in argon-purged 1 M NaOH ($T = 25°C$, $v = 1$ mV s^{-1}) for various $NiMnO_x$/C electrocatalysts containing 0.2 g Ni, dispersed on the different carbon substrates. The results are somewhat similar to those found in the literature for a MnO_2/C (C = Vulcan carbon)[28] prepared using a different thermal approach, with the voltammetric peaks associated with a series of redox processes comprising several steps with overlapped features. So, the peaks in the cyclic voltammograms may be referred to the oxidoreduction reactions of mainly MnO_2, comprising two consecutive steps involving Mn^{IV}/Mn^{III} and Mn^{III}/Mn^{II}. Coming from the more reduced states, peaks (A0/C0) probably represent the conversion/reduction of $Mn(OH)_2$ to Mn_2O_3 (or MnOOH in hydrated state), but this process must occur to a small extent because of the low intensity of the peaks. The couple (A1/C1) may involve the interconversion of $HMnO_2$ (or MnOOH)

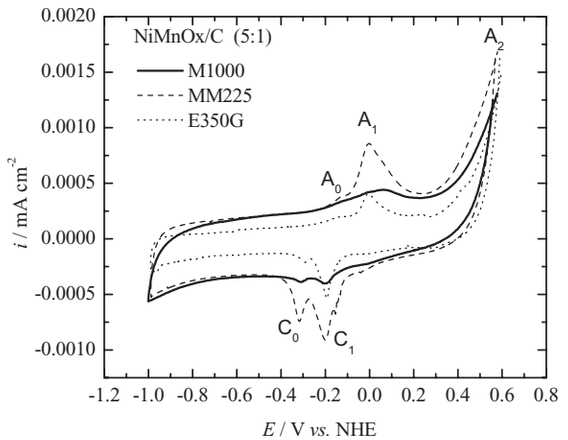

Figure 3. Cyclic voltammograms acquired in argon-purged 1 M NaOH (T = 25°C, v = 1 mV s^{-1}) for the $NiMnO_x$ 0.2 g of Ni on different carbon substrates.

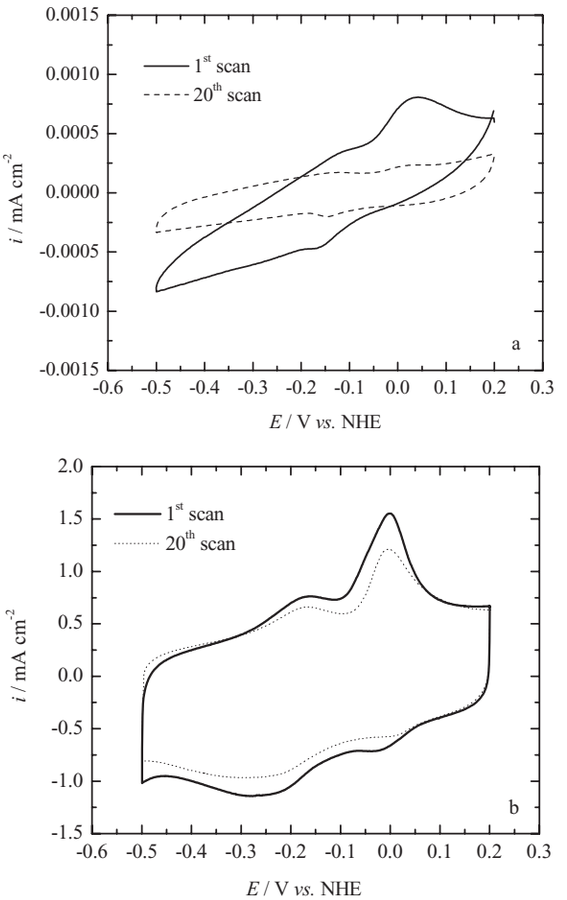

Figure 4. 1st and 20th cyclic voltammogram in argon-saturated 1 M NaOH at 25°C: (a) MnO_x/M1000 and (b) $NiMnO_x$/M1000 2.0 g Ni. Scan rate v = 5 mV s^{-1}.

to MnO_2, but it may also contain a contribution of the $Ni(OH)_2$/NiOOH redox couple (from this perspective, the small shoulder observed on the upper bound of the C1 peak on the plot for $NiMnO_x$/E350G could indeed correspond to such Ni^{III} reduction into Ni^{II}). The above well-defined proton insertion/deinsertion couple is observed in all cases, but the corresponding electrochemical features are more clearly evidenced for the catalysts formed with the E350G and MM225 carbons. The proton deinsertion/insertion process can be rationalized in terms of the general reaction

$$H_xMnO_2 + xOH^- \leftrightarrow MnO_2 + xH_2O + xe^- \quad [3]$$

which is reversible only for low hydrogen amounts into the MnO_x lattice. The changes of valence of Mn associated with the amount of proton inserted may play an important role in the electrocatalysis of the ORR by MnO_2, as already pointed out in Ref. 17. This issue will be discussed later in this work. Finally, peak (A2) must be related to the anodic decomposition of water into molecular oxygen, even if one cannot rule out any carbon corrosion at that rather high potential.

The short-term stability of the MnO_x and $NiMnO_x$ electrode surface was investigated by the electrode multiple-cycling in the alkaline solution; the results are presented in Fig. 4. For the pure MnO_x/C sample (Fig. 4a), the material undergoes irreversible reduction of metastable oxides in the ORR potential range, as revealed by the reduction peak around 0.05 V vs NHE. This yields to a fast decrease of the coulometry upon cycling, probably following dissolution of MnOOH.[17,18] An example of result for a Ni(II)-doped sample is presented in Fig. 4b, which shows the 1st and 20th voltammetric cycles in the potential range of −0.5 to 0.2 V vs NHE. Comparing this latter CV profile with that of pure MnO_x/C does confirm the better electrochemical stability of the Ni-doped MnO_x/C materials upon potential cycling in strong alkaline medium. This evidences the short-term electrochemical stability of the material, particularly related to the absence of dissolution of manganese compounds in the form of MnO_4^{2-} or MnO_4^- ions. The result agrees with that obtained for $NiMnO_x$/C materials supported onto Chezacarb carbon, both on a short-term[17,18] or long-term[29] basis. They are representative of the behavior for all the $NiMnO_x$/C electrocatalysts regardless of (i) the level of Ni-doping and (ii) the nature of the carbon substrate (CV results not shown for brevity) and confirm that Ni-adjunction within the MnO_x lattice enables to stabilize the MnO_x phases.[17,18,29]

Oxygen reduction activity.— The steady-state polarization ORR voltammograms plotted on the MnO_x/M1000 electrocatalyst at various revolution rates (Fig. 5a) illustrate the typical increase of the limiting current densities at the disk with the increase of the revolution rate, in agreement with the Levich theory. Similar oxygen reduction voltammograms for the MnO_x/M1000 materials with several Ni contents are compared in Fig. 5b. A comparison of the quasi-stationary oxygen reduction voltammograms at 1600 rpm for the $NiMnO_x$-based electrocatalysts with several carbon substrates is made in Fig. 6, while Table III summarizes the values of the ORR onset and H-insertion onset potentials on the several electrocatalysts.

The results of Fig. 5b put into evidence that increasing the level of Ni-doping in these MnO_x/M1000 electrocatalysts only has a slight influence on the ORR onset potential. More specifically, Table III points toward a small but non-negligible effect of the 0.1 g Ni-doping on the electrocatalytic activity (SA and MA) values of $NiMnO_x$/M1000, but this beneficial effect over pure MnO_x/M1000 levels off at increasing Ni-doping level (it monotonously decrease from 0.2 to 2 g Ni-doping). On the contrary, a clear increase of the limiting current is noted in Fig. 5b, putting into evidence the favorable effect of increasing Ni-doping level (in the range surveyed here) with respect to the number of electrons involved in the ORR. This is also confirmed by the Koutecky–Levich analysis of Table IV.

It is wise to point out here that great care was devoted to the $NiMnO_x$/C-based TPC active layer preparation: All the layers exhibited similar thickness and lateral extension. Therefore, the limiting current increase observed here can clearly be attributed to a change in the ORR mechanism more than to any mass-transport/residence-time effect within the TPC.

Figure 6 and Table III confirm that in the present experimental

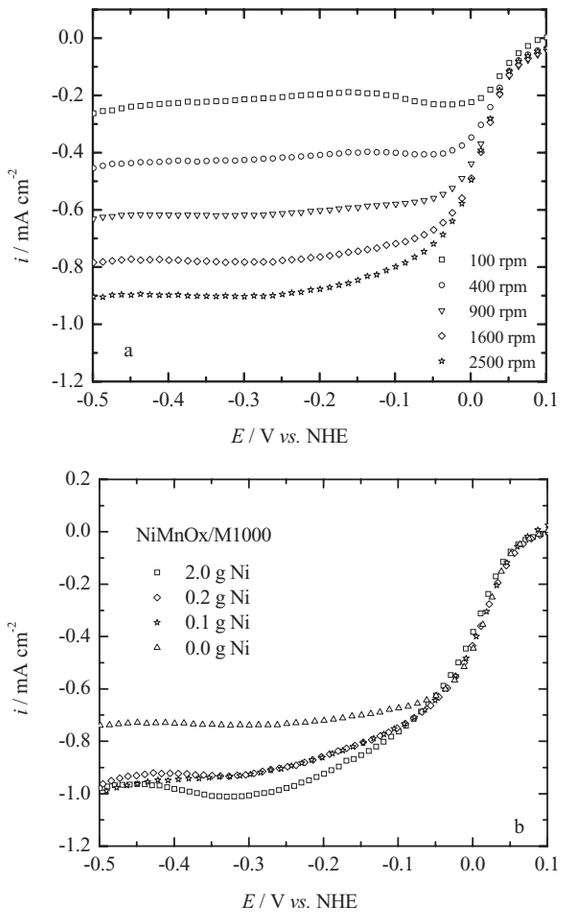

Figure 5. (a) Oxygen reduction voltammograms plotted on the MnO_x/M1000 electrocatalyst at various speed rotation and (b) oxygen reduction voltammograms plotted on various $NiMnO_x$/M1000 electrocatalysts in 1 M NaOH at 25°C, ω = 1600 rpm at v = 5 mV s^{-1}.

conditions, the onset potentials for the oxygen reduction reaction are rather similar for both the MnO_x and $NiMnO_x$ materials, regardless of the nature of the carbon substrate used. However, it is clearly noted in Fig. 6 that when MM225 and E350G carbons are used, the limiting current densities are higher when compared to those with M1000.

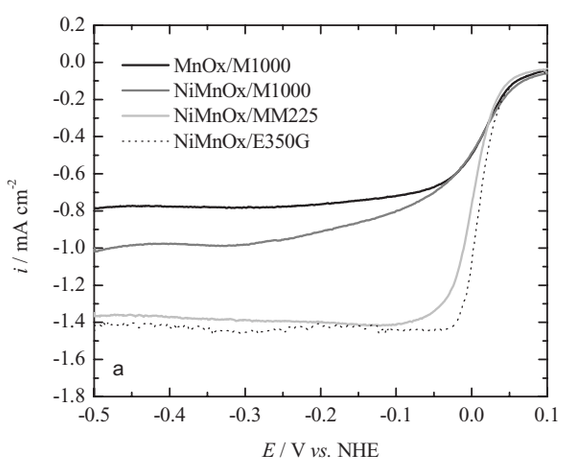

Figure 6. Oxygen reduction voltammograms in 1 M NaOH at 25°C (v = 5 mV s^{-1}) for several $NiMnO_x$ 0.2 g Ni electrocatalysts at ω = 1600 rpm.

For conducting a more specific comparison of the catalytic activity, the values of the MA and SA toward ORR at 0.0 V vs NHE were calculated by using the equivalent MnO_2 loadings (Table II) for all catalysts. These values, presented in Table III, confirm that the mass and specific activities of the manganese oxides decrease with the increase of the Ni-doping level for all carbon substrates. However, it is clearly noted that the $NiMnO_x$/MM225 and $NiMnO_x$/E350G electrocatalysts present higher values toward ORR compared to M1000. This is probably a consequence of their higher specific surfaces as compared to M1000 (Table I). The presence of different phases of Mn oxides in the $NiMnO_x$/MM225 and $NiMnO_x$/E350G materials compared to M1000 may also explain such overall enhanced ORR activity.

A mechanistic analysis of the ORR in several catalysts was made in terms of mass-transport-corrected Tafel plots[30] (E vs $\log[i_k = (i \times i_d)/(i_d - i)]$, where i_d is the diffusion limiting current) and from Levich plots, as shown in Figs. 7 and 8, respectively. The Tafel plots were used to obtain the Tafel coefficients for the ORR, while the Levich lines were employed to estimate the number of electrons involved in the reaction;[12] these results are summarized in Table IV.

The results of Fig. 7 confirm the rather identical bulk kinetic activity of the various manganese oxide-based materials. However, there are important differences in the values of the Tafel slopes, whose values ranged from ca. 90–110 mV dec^{-1} for the M1000-based materials to 40–55 mV dec^{-1} for the MM225 and E350G electrocatalysts, independent of the Ni content. These results would evidence small participation of the carbon particles in the oxygen reduction electrocatalysis for the M1000 carbon, while in the other two cases the participation may be more significant: The Tafel slopes is close to that of pure carbon (~ 30 mV dec^{-1}).[28] This observation is consistent with the large surface area of these carbon materials (Table I). The presence of different phases of Mn oxides in the $NiMnO_x$/MM225 and $NiMnO_x$/E350G materials compared to M1000 may also be responsible for the differences in the Tafel slopes.

Table IV shows that for the M1000-based material and at potential corresponding to the limiting current plateaus, there is a clear effect of the Ni content in the number of electrons involved in the ORR, which increases from two in the absence of Ni to near three for 2.0 wt % of Ni. In the cases of the catalysts with the MM225 and E350G carbons, the number of electrons is closer to four, independent of the Ni content.

So, as proposed for other Mn oxide materials,[28] one would conclude that all the $NiMnO_x$/C materials would reduce oxygen with peroxide formation at high potential (low ORR overpotential)

$$O_2 + H_2O + 2e^- \rightarrow HO_2^- + OH^- \quad [4]$$

followed by heterogeneous catalytic chemical disproportionation reaction of HO_2^-

$$2\ HO_2^- \rightarrow O_2 + 2\ OH^- \quad [5]$$

The extent of such heterogeneous catalytic chemical disproportionation reaction depends on the catalyst. It may ultimately result in an overall four-electron process per O_2 molecule if HO_2^- is completely disproportionated and the O_2 fully recycled back to the electrode (within the TPC layer).

The results of Table IV for M1000 show that, in absence of Ni, only the peroxide formation step takes place, with the occurrence of the disproportionation reaction progressively increasing as a function of the increase of the Ni content. However, this reaction never occurs to a full extent. In the case of the MM225 and E350G carbons, the disproportionation reaction seems to occur at large rates, thus providing the complete recycling of O_2 and leading an overall four-electron pathway. It is likely that the higher specific area for these carbons than for M1000 enables the trapping of hydrogen

Table III. MA and SA calculated at 0.0 V vs NHE for the MnO_x/C-based materials. The onsets for the ORR and the H-insertion reaction are also provided, when available.

Catalysts	MA (mA g^{-1})		SA (mA cm^{-2})	Onset ORR (V vs NHE)	Onset H insertion (V vs NHE)
MnO_x/M1000	MnO_2	MnO_2 + Ni			
2.0 g Ni	8.42	7.22	0.004	0.075	0.05
1.0 g Ni	10.6	9.86	0.005	0.078	0.06
0.5 g Ni	14.1	13.3	0.007	0.080	0.05
0.3 g Ni	19.4	18.7	0.009	0.082	0.05
0.2 g Ni	16.1	15.7	0.008	0.082	0.05
0.1 g Ni	24.8	24.5	0.010	0.103	0.05
0.0 g Ni	10.8	—	0.003	0.098	0.01
MM225-0.2 g Ni	13.6	13.4	0.006	0.073	0.02
MM225-0.1 g Ni	65.5	64.9	0.030	0.076	0.02
E350G-0.2 g Ni	80.0	79.3	0.040	0.074	0.05
E350G-0.1 g Ni	58.1	57.5	0.030	0.076	0.05
MnO_x/Chezacarb[a]	11.3	—	0.004	—	
$NiMnO_x$/Chezacarb[b]	39.6	—	0.020	—	
MnO_2/Vulcan XC72[b]	0.37	—	—	—	
Mn_2O_3/Vulcan XC72[b]	0.03	—	—	—	
Mn_3O_4/Vulcan XC72[b]	0.12	—	—	—	
10 wt % Pt/Vulcan XC72[a,c]	40.1	—	—	—	

[a] Measured in 1 M KOH at 25°C from Ref. 17.
[b] Recalculated from Ref. 27.
[c] MA expressed per g Pt.

peroxide more easily within the active layer structure, thereby increasing the probability for their catalytic decomposition on $NiMnO_x$ nanoparticles. In addition, an important observation to be made is that, in accordance with the results of Fig. 1, the occurrence of disproportionation reaction seems to be more favorable when $NiMnO_x$/C catalysts with agglomerated-like structures are present.

Conclusions

The catalytic activity of Ni-doped MnO_x catalysts supported on different carbon powder substrates [Monarch 1000 (M1000), from Cabot, and MM225 or E350G, both from Timcal] was investigated so as to characterize the effects of these substrates toward the ORR kinetics in alkaline medium. The physicochemical characterization results (TEM and XRD) have evidenced small insertion of the Ni atoms in the MnO_x structure, with the $NiMnO_2$ phase present in form of needles or agglomerates with crystallites sizes on the order of 1.5–6.7 nm. The presence of a layered manganite (MnOOH) phase has been detected for the M1000-supported $NiMnO_x$ material, while this manganite phase was absent for the E350G and MM225 carbons. In addition, species differing from the MnO_x main phase are (very moderately) present for the E350G and MM225 carbons.

Table IV. ORR Tafel slope in the low overpotential region and number of electrons exchanged per O_2 species at −0.4 V vs NHE for several $NiMnO_x$/C electrocatalysts in 1 M sodium hydroxide.

Catalysts	b (V dec^{-1})	n (−0.4 V vs NHE)
MnO_x/M1000	0.069	2.0
2.0 g Ni	0.093	3.1
1.0 g Ni	0.119	2.9
0.5 g Ni	0.115	2.7
0.3 g Ni	0.110	2.4
0.2 g Ni	0.092	2.5
0.1 g Ni	0.102	2.5
MM225-0.2 g Ni	0.051	3.7
MM225-0.1 g Ni	0.036	3.2
E350G-0.2 g Ni	0.054	3.9
E350G-0.1 g Ni	0.053	3.8

The oxygen reduction reaction is somewhat faster for slightly Ni-doped MnO_x/M1000, but higher Ni-doping levels are not beneficial. For the catalysts with M1000 substrate, it is clearly noted that in the absence of Ni, the ORR just follows the peroxide formation step, with the occurrence of a HO_2^- disproportionation reaction to a small extent. This chemical reaction is progressively increasing with higher Ni-doping levels but never occurs quantitatively. In the case of the materials with the MM225 and E350G carbons, the disproportionation reaction occurs at larger rates, thus providing the complete recycling of O_2 and leading to an overall four-electron ORR pathway. The MM225- and E350G-supported $NiMnO_x$ catalysts also display faster ORR kinetics than those supported onto M1000.

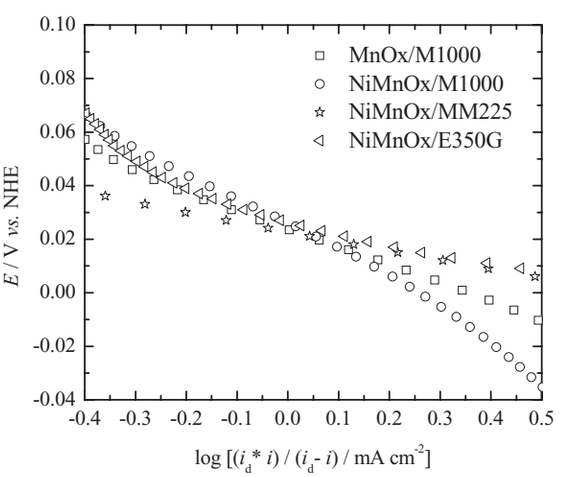

Figure 7. Mass-transport-corrected Tafel plots for the ORR in the MnO_x/C and Ni–MnO_x/C (0.2 g Ni) electrocatalysts. 1 M NaOH at 25°C, ω = 1600 rpm at 5 mV s^{-1}.

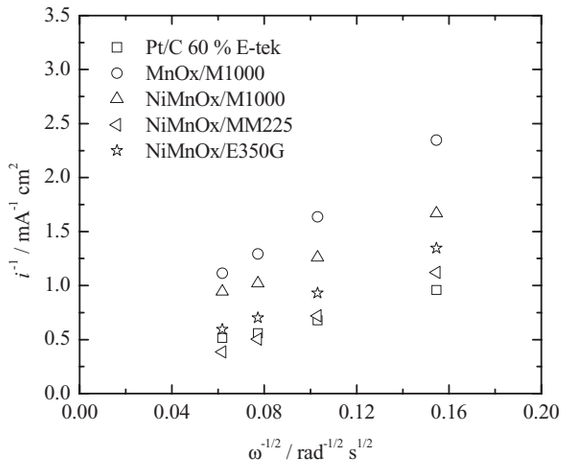

Figure 8. Levich plots for the MnO_x-based 0.2 g Ni electrocatalysts obtained at $E = -0.4$ V vs NHE.

Acknowledgments

The authors thank J. Vondràk's group in the Czech Academy of Science for precious advice and fruitful discussions. Capes/Cofecub is also acknowledged for financing (project Ph 598/08).

Centre National de la Recherche Scientifique assisted in meeting the publication costs of this article.

References

1. S. Srinivasan, *J. Electrochem. Soc.*, **136**, 41C (1989).
2. C. Chakkaravarth, A. K. Abdul Waheed, and H. V. K. Udupa, *J. Power Sources*, **6**, 203 (1981).
3. K. Kinoshita, *Electrochemical Oxygen Technology*, John Wiley & Sons, New York (1992).
4. M. Chatenet, M. Aurousseau, R. Durand, and F. Andolfato, *J. Electrochem. Soc.*, **150**, D47 (2003).
5. L. Swette and N. Kackley, *J. Power Sources*, **29**, 423 (1990).
6. J. Kivisaari, J. Lamminen, J. Lampinen, and M. Viitanen, *J. Power Sources*, **32**, 223 (1990).
7. M. L. Calegaro, F. H. B. Lima, and E. A. Ticianelli, *J. Power Sources*, **158**, 735 (2006).
8. J.-P. Brenet, *J. Power Sources*, **4**, 183 (1979).
9. J. P. Hoare, *The Electrochemistry of Oxygen*, p. 13, John Wiley & Sons, New York (1968).
10. T. Yano, D. A. Tryk, K. Hashimoto, and A. Fujishima, *J. Electrochem. Soc.*, **145**, 1870 (1998).
11. T. Yano, E. Popa, D. A. Tryk, K. Hashimoto, and A. Fujishima, *J. Electrochem. Soc.*, **146**, 1081 (1999).
12. L. Mao, D. Zhang, T. Sotomura, K. Nakatsu, N. Koshiba, and T. Ohsaka, *Electrochim. Acta*, **48**, 1015 (2003).
13. J. Vondràk, M. Sedlarikovà, and V. Novàk, *J. New Mater. Electrochem. Syst.*, **1**, 25 (1998).
14. B. Klápště, J. Vondrák, and J. Velická, *Electrochim. Acta*, **47**, 2365 (2002).
15. R. F. Scarr, J. C. Hunter, and P. J. Slezack, in *Handbook of Batteries*, Chap. 10, D. L. Linden and T. B. Reddy, Editors, McGraw-Hill, New York (2002).
16. J. Vondrák, B. Klápště, J. Velická, M. Sedlaříková, V. Novàk, and J. Reiter, *J. New Mater. Electrochem. Syst.*, **8**, 1 (2005).
17. I. Roche, E. Chainet, M. Chatenet, and J. Vondrák, *J. Phys. Chem. C*, **111**, 1434 (2007).
18. J. Vondrák, B. Klápště, J. Velická, M. Sedlaříková, J. Reiter, I. Roche, E. Chainet, J.-F. Fauvarque, and M. Chatenet, *J. New Mater. Electrochem. Syst.*, **8**, 209 (2005).
19. P. Bezdicka, T. Grygar, B. Klápště, and J. Vondrák, *Electrochim. Acta*, **45**, 913 (1999).
20. F. Maillard, A. Bonnefont, M. Chatenet, L. Guétaz, B. Doisneau-Cottignies, H. Roussel, and U. Stimming, *Electrochim. Acta*, **53**, 811 (2007).
21. M. Chatenet, L. Geniès-Bultel, M. Aurousseau, R. Durand, and F. Andolfatto, *J. Appl. Electrochem.*, **32**, 1131 (2002).
22. PINE Instrument Company, http://www.pineinst.com/echem/index.asp, Rotated Ring-Disk Electrodes, DT21 Series Single-Piece., last accessed Dec. 2010
23. A. J. Bard and L. R. Faulkner, *Electrochimie—Principes, Méthodes et Applications*, Masson, Paris (1983).
24. M. Chatenet, M. Aurousseau, and R. Durand, *Ind. Eng. Chem. Res.*, **39**, 3083 (2000).
25. M. Chatenet, M. Aurousseau, and R. Durand, *Electrochim. Acta*, **45**, 2823 (2000).
26. V. M. M. Lobo, in *Handbook of Electrolyte Solutions*, V. M. M. Lobo, Editor, Physical Science Data 41A, Elsevier, Amsterdam (1989).
27. A. R. West, in *Solid State Chemistry and Its Applications*, p. 742, John Wiley & Sons, New York (1984).
28. F. H. B. Lima, M. L. Calegaro, and E. A. Ticianelli, *Electrochim. Acta*, **52**, 3732 (2007).
29. I. Roche, E. Chaînet, M. Chatenet, and J. Vondrák, *J. Appl. Electrochem.*, **38**, 1195 (2009).
30. J.-P. Diard, B. Le Gorrec, and C. Montella, in *Cinétique Electrochimique*, Herman, Paris (1996).